Nb_2O_5 Nanostructures as Precursors of Cycling Catalysts for Hydrogen Storage in MgH_2

Xin Zhang,‡ Xuelian Zhang,‡ Lingchao Zhang, Zhenguo Huang, Limei Yang, Mingxia Gao, Changdong Gu, Wenping Sun, Hongge Pan, Yongfeng Liu**

Xin Zhang - State Key Laboratory of Silicon and Advanced Semiconductor Materials, Key Laboratory of Advanced Materials and Applications for Batteries of Zhejiang Province and School of Materials Science and Engineering, Zhejiang University, Hangzhou 310058, China.

Xuelian Zhang - State Key Laboratory of Silicon and Advanced Semiconductor Materials, Key Laboratory of Advanced Materials and Applications for Batteries of Zhejiang Province and School of Materials Science and Engineering, Zhejiang University, Hangzhou 310058, China.

Lingchao Zhang - State Key Laboratory of Silicon and Advanced Semiconductor Materials, Key Laboratory of Advanced Materials and Applications for Batteries of Zhejiang Province and School of Materials Science and Engineering, Zhejiang University, Hangzhou 310058, China.

Zhenguo Huang - School of Civil & Environmental Engineering, University of Technology Sydney, 81 Broadway, Ultimo, NSW, 2007, Australia.

Limei Yang - School of Civil & Environmental Engineering, University of Technology Sydney, 81 Broadway, Ultimo, NSW, 2007, Australia.

Mingxia Gao - State Key Laboratory of Silicon and Advanced Semiconductor Materials, Key Laboratory of Advanced Materials and Applications for Batteries of Zhejiang Province and School of Materials Science and Engineering, Zhejiang University, Hangzhou 310058, China.

Changdong Gu - State Key Laboratory of Silicon and Advanced Semiconductor Materials, Key Laboratory of Advanced Materials and Applications for Batteries of Zhejiang Province and School of Materials Science and Engineering, Zhejiang University, Hangzhou 310058, China.

Wenping Sun - School of Materials Science and Engineering, Zhejiang University, Hangzhou 310027, China.

Hongge Pan - State Key Laboratory of Silicon and Advanced Semiconductor Materials, Key Laboratory of Advanced Materials and Applications for Batteries of Zhejiang Province and School of Materials Science and Engineering, Zhejiang University, Hangzhou 310058, China; Institute of Science and Technology for New Energy, Xi'an Technological University, Xi'an, 710021, China.

Yongfeng Liu - State Key Laboratory of Silicon and Advanced Semiconductor Materials, Key Laboratory of Advanced Materials and Applications for Batteries of Zhejiang Province and School of Materials Science and Engineering, Zhejiang University, Hangzhou 310058, China; Institute of Science and Technology for New Energy, Xi'an Technological University, Xi'an, 710021, China.

ABSTRACT: High operation temperatures and sluggish kinetics are major obstacles for the practical applications of MgH_2 as a solid hydrogen carrier. Introducing nanoscaled high-activity catalysts has been effective in improving hydrogen cycling of MgH_2. However, it remains still unclear that between nanoparticle size and morphology, which one is the decisive factor of the catalytic activity of a given catalyst. In this work, we studied this topic by taking nanostructured niobium oxide (Nb_2O_5) as a representative sample. Five types of Nb_2O_5 catalytic additives with different morphologies and nanosizes were synthesized and their catalytic activities were compared with commercial microparticles. Our results unambiguously demonstrate that the catalytic activity of Nb_2O_5 is determined by the primary particle size rather than the morphology and structure, because the ultrasmall Nb_2O_5 nanoparticles measured ~5 nm in size enable dehydrogenation of MgH_2 starting at 165 ºC after 1-cycle activation. The smaller nanoparticle sizes not only enhance the reactivity of Nb_2O_5 but also lead to more uniform dispersion when ball milled with MgH_2, which enable in-situ formation of more homogeneous and finer Nb-based active species, therefore much higher catalytic activity. This important insight will guide the design and optimization of novel high-activity catalysts toward hydrogen cycling of MgH_2 and other hydrogen storage materials.

KEYWORDS: hydrogen storage, MgH_2, morphology, particle size, catalytic activity

Table of Contents Image:

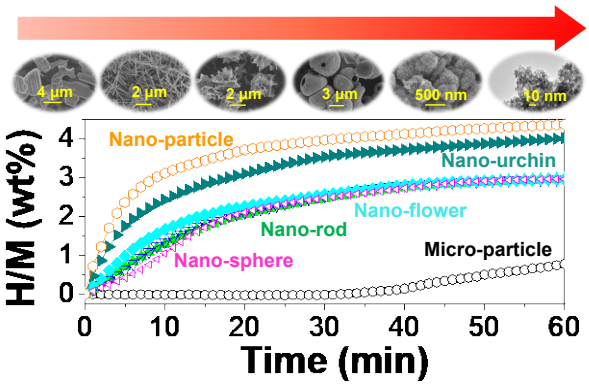

INTRODUCTION

There is arguably the greatest expectation for hydrogen to facilitate the realization "net zero" as an ideal green energy carrier.[1-3] However, it has been challenging to find a compact, safe and cost-effective manner to store and transport hydrogen at scale.[4-6] With respect to compressed and liquefied H_2, metal hydrides are generally accepted as a preferable option because of their high gravimetric and volumetric hydrogen densities and low operating pressures.[7-13] Many metals and alloys can react with hydrogen to form metal hydrides.[14-17] Magnesium hydride (MgH_2), with 7.6 wt% of hydrogen capacity and good reversibility, has attracted considerable attention as a solid hydrogen carrier.[18-20] Unfortunately, its applications have been heavily limited by high operation temperatures and sluggish kinetics caused by high thermodynamic and kinetic barriers.

The introduction of a suitable catalyst or catalytic additive is the simplest and most effective way to reduce the operating temperatures and enhance the reaction kinetics for hydrogen storage in the Mg/MgH_2 system.[21-24] Over the past few decades, various catalysts and catalytic additives have been developed to improve the hydrogen storage performance of MgH_2, including transition metal and its alloys (e.g. Ti, V, Nb, Ni, ZrNi, Ti_2Ni, $ZrMn_2$), metal hydrides (e.g. TiH_2, ZrH_2, NbH_x, VH_x), metal halides (e.g. NbF_5, $TiCl_3$, TiF_3, $ZrCl_4$), metal oxides (e.g. TiO_2, ZrO_2, Nb_2O_5, V_2O_3), metal carbides (e.g. Ti_3C_2, Nb_4C_3), sulfides (e.g. NiS), nitrides (e.g. NbN), phosphides (e.g. Ni_2P), and carbon-based materials (e.g. carbon nanotubes, graphene).[25-54] Considerable work has also revealed that nano-sized catalysts usually delivered much enhanced catalytic activity than their bulk counterparts.[21,23,27-29] Chen et al. reported that the introduction of 4 mol% porous Ni nanofibers dramatically reduced the dehydrogenation peak temperature from 385 °C to 244 °C, while it was only decreased to 340 °C when 4 mol% Ni powders were introduced.[27] By doping V nanosheets, Lu et al. observed the hydrogen release at 187.5 °C, but no hydrogen was detected

when using bulk V as additives even heating to 270 °C.[28] The dehydrogenation peak temperature of nanoscale $ZrMn_2$ modified MgH_2 was only 250.8 °C, which was 70 and 103 °C lower than those of the micron-sized $ZrMn_2$ containing MgH_2 and pristine MgH_2, respectively.[29] Our recent results also indicated that the hydrogen desorption/absorption performances of nano-ZrO_2-modified MgH_2 ball milled for only 3 h largely outperformed MgH_2 ball milled with bulk-ZrO_2 for 12 h.[41]

As a result, the recent research focus has been devoted to synthesizing various nanostructured catalysts to further increase their catalytic activity. For instance, Zhang et al. synthesized $Na_2Ti_3O_7$ nanotubes (NTs) with a diameter of 10 nm and $Na_2Ti_3O_7$ nanorods (NRs) with diameters of 100–500 nm.[55] The MgH_2-$Na_2Ti_3O_7$ NT and MgH_2-$Na_2Ti_3O_7$ NR composites were observed to desorb 6.5 wt% H_2 within 6 min and 16 min at 300 °C, respectively. The nanoflower-like $Na_2Ti_3O_7$-containing MgH_2 released 6.6 wt% H_2 within 4 min at 260 °C.[56] The addition of 5 wt% TiO_2 nanosheets (NS) with exposed {001} facets reduced the onset and peak dehydrogenation temperatures of MgH_2 to 180.5 °C and 220.4 °C, respectively, and approximately 6.0 wt% H_2 was liberated within 3.2 min at 260 °C.[57] Similarly, the two-dimensional graphene-like TiO_2 (TiO_2 (B)) also effectively enhanced the hydrogen storage performances of MgH_2 because the MgH_2+10 wt% TiO_2 (B) sample desorbed hydrogen starting at ~200 °C with a peak desorption temperature as low as 227.6 °C.[40] Hydrogen release amounted to 6.16 wt% in 10 min at 250 °C. The hierarchical porous $TiNb_2O_7$ microspheres built with 20–50 nm primary nanospheres enabled 177 °C of onset desorption temperature of MgH_2 and 5.5 wt% of hydrogen release in 10 min at 250 °C.[58] The fully dehydrogenated sample re-absorbed 4.5 wt% H_2 within 3 min at 150 °C. More encouragingly, the two-dimensional nanoflake-shape $TiNb_2O_7$ with 3 wt% loading successfully reduced the dehydrogenation onset temperature to 178 °C and the dehydrogenated sample was fully hydrogenated at 150 °C within 15 minutes under 50 bar H_2.[59] The outstanding catalytic activity

was attributed to the extremely high surface area, porous structure, low crystallinity, and preferential exposure of (110) facet of the $TiNb_2O_7$ nanoflakes. As it stands now, nanostructured catalysts display much higher catalytic activity for hydrogen storage in MgH_2. However, it is still unclear that between structure, morphology and nanosize, which one plays more dominant catalytic roles for a given catalyst in the solid-state hydrogen storage field.

In this work, to elucidate the decisive factors of the catalytic activity, we take Nb_2O_5, one of the most studied catalysts, as a representative example and fabricate five types of nanostructures with different nanosizes, structures and morphologies and compare their catalytic effects in hydrogen storage of MgH_2 with commercial microparticles. The results indicate that the catalytic activity of Nb_2O_5 strongly depends on its primary nanoparticle size rather than its structure and morphology. The decreased particle size not only increases the reaction activity of Nb_2O_5 but also facilitates the dispersion. This gives rise to in-situ formation of much finer and more homogeneous distribution of Nb-based active species after ball milling with MgH_2, consequently higher catalytic activity. This work gives important insights into the design and fabrication of catalysts for hydrogen storage in light-metal hydrides.

EXPERIMENTAL SECTION

Synthesis of Nb_2O_5. Five types of Nb_2O_5 nanostructures with different structures, morphologies and sizes, including nanoflowers, nanorods, hollow spheres, sea urchins and nanoparticles, were fabricated as follows.

(1) Nanoflower-like Nb_2O_5 (f-Nb_2O_5): The f-Nb_2O_5 was synthesized using a typical hydrothermal process followed by calcination. First, 1.0 g of $NbCl_5$ (Alfa Aesar, 99.95%) was dissolved in 10 mL absolute ethanol and then mixed with 50 mL 4 wt% ammonia water. After

stirring for 2 h, the white precipitates were centrifuged and separated with an H1750 high speed centrifuge (Xiangyi Instrument Plant, China). The centrifuged product was dispersed in 70 mL deionized water. Owing to the residual NH_4^+, the pH value of the solution was between 9-10. The mixed solution was transferred to a 100 mL Teflon-lined autoclave and kept at 240 °C for 24 h for hydrothermal reaction. The resulting precipitates were collected via centrifugation, washing with deionized water and freeze drying. The thus obtained product was the precursor of Nb_2O_5 nanoflowers, denoted as p-f-Nb_2O_5. The final Nb_2O_5 nanoflowers were obtained by calcining p-f-Nb_2O_5 at 600 °C for 1 h in air, which was denoted as f-Nb_2O_5.

(2) Nanorod-like Nb_2O_5 (r-Nb_2O_5): The preparation process of r-Nb_2O_5 is similar to that of p-f-Nb_2O_5. The difference is that the precipitation formed after adding ammonia water was washed several times with deionized water, and then dispersed in deionized water with the pH value of the solution being 7-8. After the hydrothermal reaction similar to that of p-f-Nb_2O_5, nanorod-like Nb_2O_5 was obtained.

(3) Hollow sphere-like Nb_2O_5 (s-Nb_2O_5): The Nb_2O_5 hollow spheres were prepared by using a typical two-step process described in our previous report.[60] The resulting product was referred as s-Nb_2O_5.

(4) Urchin-like Nb_2O_5 (u-Nb_2O_5): To prepare u-Nb_2O_5, 2.0 g ammonium niobite oxalate hydrate (Sigma Aldrich, 99.99%) was first dissolved in 25 mL deionized water and then added 10 mL 30% H_2O_2 solution. The mixed solution was transferred to a 50 mL autoclave for the hydrothermal reaction at 160 °C for 6 h. The solid products were isolated by centrifugation, washing several times with deionized water, and finally freeze-dried to produce the white powders of u-Nb_2O_5.

(5) Nanoparticulate Nb_2O_5 (NP-Nb_2O_5): The typical preparation procedure of NP-Nb_2O_5 includes: i) dissolving 500 mg of $NbCl_5$ (Alfa Aesar, 99.95%) in 60 mL absolute ethanol first and

then adding 10 mL glacial acetic acid and 1 mL deionized water; ii) heating the solution in an autoclave at 200 °C for 48 h; iii) isolating solids by centrifugation and washing with deionized water; and iv) freeze-drying the solids to obtain NP-Nb_2O_5.

Preparation of Nb_2O_5 modified MgH_2. The prepared Nb_2O_5 was mixed with MgH_2 at a mass percentage of 7%. MgH_2 with 97% of purity was synthesized in our own laboratory as reported previously.[35] Mechanical ball milling was conducted to mix Nb_2O_5 and MgH_2 on a QM-3SP4 planetary ball mill (Nanjing Nanda Instrument Plant, China) at 500 rpm for 3 h. The 304 stainless steel milling jar and balls were used and the ball-to-sample weight ratio was about 120:1. The milling jar was first vacuumed and then filled with 10 bar H_2 before milling operation. No metal contaminations were found in the post-milled samples (Figure S1). All the sample handling was carried out in an Etelux Lab2000 glove box filled with high-purity Ar. As a comparison, the high-purity MgH_2 (purity: 99.99%) was obtained from Center of Hydrogen Science at Shanghai Jiaotong University.

Characterization. X-ray diffraction (XRD) analysis was carried out on Rigaku MiniFlex 600 (Japan) with Cu K_α radiation operated at 40 kV and 15 mA with a scanning rate of 5° min^{-1}. A custom-designed sample holder covered with Scotch tape was used to prevent exposure of samples to air and moisture during the tests. Scanning electron microscope (SEM, Hitachi SU8010) and transmission electron microscope (TEM, FEI Tecnai G2 F20 S-TWIN) were employed to observe morphologies and analyze microstructures. The specific surface areas of the samples were determined using Brunauer-Emmet-Teller (BET) method based upon nitrogen adsorption–desorption data collected on Quantachrome Nova 1000e analyzer. Elemental distribution was analyzed by energy dispersive X-ray spectrometer (EDS, X-Max) attached to the SEM and TEM facilities. X-ray photoelectron spectroscopy (XPS) measurements were performed on Thermo

Scientific ESCALAB 250Xi with a monochromatic Al Kα X-ray source (1486.6 eV) under a base pressure of ~8.8×10^{-10} mbar. The adventitious C peak at 284.8 eV was used as the reference to calibrate the XPS data. The particle size distribution of the$_2$ samples were estimated by using a nanoparticle size analyzer (Zetasizer Nano-ZS, Malvern, Britain). Typically, the samples were ultrasonically dispersed in tetrahydrofuran (THF) in the Ar-filled glovebox, and then 1 mL of solid materials suspension liquid was sealed in the quartz cell with a Teflon plug and rapidly transferred from the glovebox to the analyzer.

A home-built temperature-programmed desorption (TPD) system equipped with a mass spectrometer (MS, Hiden QIC-20) was used to characterize dehydrogenation behavior. Approximately 15 mg of sample was loaded into a stainless-steel tube reactor and heated from ambient temperature to the desired temperatures at a preset heating rate with Ar as a carrier gas. The quantitative measurements of hydrogen desorption and absorption were conducted on a homemade Sievert's type apparatus. In these experiments, ~65 mg of sample was weighed for measurements. For non-isothermal tests, the sample was heated with a heating rate of 2 °C min^{-1} under initial vacuum. The dehydrogenated sample was rehydrogenated from room temperature to 250 °C at 1 °C min^{-1} with an initial hydrogen pressure of 50 bar (purity: 99.9999%). For isothermal experiments, the sample was first quickly (10 °C min^{-1} of heating rate) heated to the desired temperature and then dwelled for a certain duration at this temperature. Hydrogen cycling measurements were carried out at 260 °C and 50 bar of hydrogen pressure.

RESULTS AND DISCUSSION

Structure and morphology of various Nb_2O_5. Nb_2O_5 nanostructures with various microstructures and nanosizes were synthesized by using different raw materials and reaction

conditions, as schematically demonstrated in Figure 1. The resultant solid powder products were collected and subjected to XRD characterization. Figure 2 shows the XRD patterns of the as-synthesized Nb_2O_5 nanostructures and commercial microparticles. In contrast to the commercially purchased Nb_2O_5 (denoted as c-Nb_2O_5) with monoclinic structure (PDF: 37-1468) (Figure 2a), the as-synthesized Nb_2O_5 was identified to adopt orthorhombic structure (PDF: 27-1003) for nanoflowers (f-Nb_2O_5, Figure 2b), hollow spheres (s-Nb_2O_5, Figure 2c), urchin shape (u-Nb_2O_5, Figure 2d) and nanoparticles (NP-Nb_2O_5, Figure 2e), and hexagonal structure (PDF: 07-0061) for nanorods (r-Nb_2O_5, Figure 2f). The formation of different crystal structures is related to their preparation conditions, especially pH values and sintering temperatures. The precursor of Nb_2O_5 nanoflowers (denoted as p-f-Nb_2O_5) was identified to be $Nb_2O_5 \cdot 1.2H_2O$, based upon the XRD pattern (Figure S2).[61] The particularly strong reflection at $2\theta \approx 6.0°$ suggested a multi-layer structure for the p-f-Nb_2O_5.[61] The commercial sample, nanoflower-, nanorod- and hollow sphere-like samples all display quite strong and sharp diffraction peaks in their XRD profiles. However, the XRD reflections of urchin-like sample and nanoparticles are distinctly broad and weak, possibly due to their reduced grain sizes, which is verified by SEM and TEM analysis as discussed below.

Figures 3 and 4 display SEM and TEM images of commercial and the as-prepared Nb_2O_5 powders. As shown in Figure 3a, c-Nb_2O_5 consists of very irregularly shaped particles in micrometer size (~5-10 μm). r-Nb_2O_5 was measured to be several microns in length and 50-200 nm in diameter (Figure 3b). The hollow s-Nb_2O_5 was measured to be several microns in the sphere diameter (Figure 3c) and the holes are visible on the shell of these microspheres, consistent with our previous report.[60] The inner surface of the hollow spheres is relatively smooth, and the outer surface seems to be rough. The thickness of the sphere shell was determined to be around 200 nm.

The morphologies of p-f-Nb_2O_5 and f-Nb_2O_5 are shown in Figures 4a-c and Figures 4d-f, respectively. Two samples display well-defined flower-like morphology by the agglomeration of nanosheets. The slight difference was observed in their TEM images. For p-f-Nb_2O_5, the diameters of flowers are approximately 3-6 μm (Figures 4a-b) and the petals are composed of many irregular nanosheets (Figure 4c), which is responsible for the strong reflection in the XRD profile at the low angle (Figure S2). The selected area electron diffraction (SAED) pattern exhibits typical polycrystalline diffraction rings, as observed in the inset of Figure 4c. After calcining p-f-Nb_2O_5 at 600 °C for 1 h, the appearance maintains nearly the same (Figure 4d). However, the size of f-Nb_2O_5 is slightly smaller than that of p-f-Nb_2O_5 (Figures 4d-e). The petals after calcination became thinner and were even broken. The SAED pattern reveals a well-crystallized structure (Figure 4f). The SEM and TEM images of u-Nb_2O_5 are presented in Figures 4g-i. The hairy balls have porous network and the diameters of the hairy ball are about 200-500 nm. These hairy balls are composed of a large number of nanorods stacked together in disorder as observed through TEM. The diameters of nanorods were measured to be about 5-10 nm. The NP-Nb_2O_5 prepared in this work consists of numerous ultrasmall primary nanoparticles measured ~5 nm in size (Figures 4j-l). The diffuse annular halo observed in the SAED pattern indicates the poor crystallinity of NP-Nb_2O_5, agreeing well with the result of XRD analysis (Figure 2e).

The specific surface areas of various Nb_2O_5 were further measured by BET method. The results are shown in Figure S3. It is noted that the specific surface areas of f-Nb_2O_5, r-Nb_2O_5, s-Nb_2O_5 and p-f-Nb_2O_5 are very close, between 15-20 m^2/g, while those of u-Nb_2O_5 and NP-Nb_2O_5 are larger, being 158 and 275.6 m^2/g, respectively, indicating their smaller particle sizes. Table S1 summarizes and compares the crystal structures, morphology and specific surface area of

commercial and as-synthesized Nb_2O_5. Thus, Nb_2O_5 catalytic additives with various structures, morphologies and sizes have been successfully synthesized.

Catalytic effects of Nb_2O_5 on hydrogen cycling by MgH_2. NP-Nb_2O_5 was selected as an example to optimize the addition amount of catalytic additives in MgH_2. The results shown in Figure S4 indicate a remarkable low-temperature shift for the dehydrogenation curves associated with a gradual decrease in the dehydrogenation capacity when the addition of NP-Nb_2O_5 from 0 to 7 wt%. The 7 wt% NP-Nb_2O_5 addition enabled the release of 6.64 wt% H_2 at 205-330 °C, obviously lower than the desorption temperature of the post-milled pristine MgH_2 (285-385 °C). This is reasonably attributed to the catalytic effect of Nb_2O_5 rather than the size effect because of their very similar particle size after 3 h of ball milling (Figure S5). Further increasing the NP-Nb_2O_5 to 10 wt%, however, no appreciable change was observed except for an additional decrease in desorption capacity. By considering the dehydrogenation temperature and capacity, we believe that the 7 wt% NP-Nb_2O_5 addition is optimal for catalyzing hydrogen desorption from MgH_2. As a result, the catalytic effects of Nb_2O_5 with various structures, morphologies and sizes were evaluated by fabricating a series of MgH_2+7 wt% Nb_2O_5 composites via ball milling for 3 h.

Figure 5a shows the first hydrogen desorption curves of the post-milled samples measured by volumetric method. It was observed that the addition of 7 wt% Nb_2O_5 significantly reduced the dehydrogenation temperatures of MgH_2. Compared with f-Nb_2O_5, r-Nb_2O_5, s-Nb_2O_5 and p-f-Nb_2O_5, the addition of NP-Nb_2O_5 or u-Nb_2O_5 give rise to the lowest dehydrogenation temperature, indicating their much better activity in catalyzing hydrogen desorption from MgH_2, while the c-Nb_2O_5 is the least. The addition of whether NP-Nb_2O_5 or u-Nb_2O_5 significantly reduced the dehydrogenation onset temperature by ~80 °C from ~285 °C to ~205 °C at the first cycle. This is reasonably related to the apparent activation energy (E_a). As measured through Kissinger' method

(Figure S6), the E_a value of NP-Nb_2O_5-modified MgH_2 was 82.3 kJ mol^{-1}, lower than pristine MgH_2 (140.5 kJ mol^{-1}) and the samples composed of f-Nb_2O_5 (88.9 kJ mol^{-1}) and c-Nb_2O_5 (113.9 kJ mol^{-1}). More importantly, the dehydrogenation onset temperature was further lowered to ~165 °C at the second cycle (Figure 5b), possibly due to the much smaller E_a value (77.3 kJ mol^{-1}) (Figure S7). In stark contrast, c-Nb_2O_5 only induced ~50 °C of reduction in the onset dehydrogenation temperature at the first cycle and even an appreciable high-temperature shift and a much higher E_a (123 kJ mol^{-1}) at the second cycle.

Moreover, remarkable improvement was also observed for the hydrogenation steps (Figure 5c and d). The best hydrogen absorption performance was obtained for the NP-Nb_2O_5-modified sample, which commenced to absorb hydrogen at 25 °C and saturated at 150 °C with an initial hydrogen pressure of 50 bar. A nearly identical hydrogenation behavior was observed for the u-Nb_2O_5-containing sample except for a slightly high-temperature shift. In contrast, the hydrogenation of samples modified with f-Nb_2O_5, s-Nb_2O_5, r-Nb_2O_5 and p-f-Nb_2O_5 completed only when the temperature reached 250 °C. The terminal hydrogenation temperature is ~100 °C higher than that of the NP-Nb_2O_5 and u-Nb_2O_5-modified samples. For the c-Nb_2O_5-containing sample, the hydrogen uptake started at ~45 °C under 50 bar H_2 and full hydrogenation was achieved at 250 ºC. Such properties are obviously inferior to other nanostructured Nb_2O_5. The isothermal hydrogenation measured at 50 °C provided much stronger evidence for the improved kinetics. The NP-Nb_2O_5-modifed sample absorbed ~4.4 wt% H_2 within 60 min at 50 °C, and it is 4.0 wt% H_2 for the u-Nb_2O_5-containing sample under identical conditions. The amount of hydrogen uptake was measured to be 3.0 wt% for the samples modified with f-Nb_2O_5, s-Nb_2O_5, r-Nb_2O_5 and p-f-Nb_2O_5. In contrast, only ~0.5 wt% H_2 was recharged into the c-Nb_2O_5-containing

sample, which is only one-eighth of the NP-Nb_2O_5-modifed sample, indicating a relatively poorer catalytic activity of c-Nb_2O_5.

According to the above observations, we conclude that the catalytic effect of Nb_2O_5 on the hydrogen storage reaction of Mg/MgH_2 is in the following order: NP-Nb_2O_5 > u-Nb_2O_5 > f-Nb_2O_5 ≈ r-Nb_2O_5 ≈ s-Nb_2O_5 > c-Nb_2O_5. Here, it is noteworthy that in spite of different morphologies and phase structures, the f-Nb_2O_5, r-Nb_2O_5 and s-Nb_2O_5 offered nearly identical catalytic efficacy. Such tendency is consistent with the specific surface areas shown in Table S1. This fact therefore makes us believe that the primary particle size, which is directly related to specific surface area, determines the catalytic activity of Nb_2O_5, instead of the phase structure and morphology. The smaller the particle size of Nb_2O_5 is, the higher the catalytic activity for hydrogen storage in MgH_2.

Microstructure analysis of Nb_2O_5 modified MgH_2 systems. It is well known that for metal hydride-based hydrogen storage systems, the efficiency of a catalyst strongly depends on how well it is dispersed through the system. In this regard, we first characterized and compared the distribution of Nb element after ball milling Nb_2O_5 with MgH_2. Figure 6 shows SEM and EDS mapping images of the samples modified with c-Nb_2O_5, NP-Nb_2O_5 and r-Nb_2O_5 as representative examples for comparison. Strong aggregation of Nb element was observed for the c-Nb_2O_5-containing sample after ball milling (Figure 6a). For the samples modified with NP-Nb_2O_5 and r-Nb_2O_5 (Figures 6b and c), the distribution of Nb is relatively homogeneous, especially for the NP-Nb_2O_5-containing sample. This is closely related to their small primary particle sizes, which enables uniform dispersion only by the short time ball milling. Here, it should be noted that at higher magnification (Figure S8), the aggregation of Nb element to some extent is also visible for r-Nb_2O_5, which is responsible for the slightly poorer hydrogenation kinetics of the r-Nb_2O_5-modified sample with respect to the sample modified with NP-Nb_2O_5, as shown in Figures 5c and

d. In addition, those bright spots shown in SEM images (Figure 6) are correlated to Nb-based species. Backscattered electron (BSE) images shown in Figure S9 also confirm the much more uniform distribution of Nb in the u-Nb_2O_5 and NP-Nb_2O_5-containing samples, in comparison with samples containing f-Nb_2O_5, s-Nb_2O_5 and r-Nb_2O_5.

The distribution of Nb was further studied by STEM and EDS mapping analyses. As shown in Figure S10, NP-Nb_2O_5 exhibits the most homogeneous dispersion in the MgH_2 matrix followed by u-Nb_2O_5, with c-Nb_2O_5 sample featuring large agglomerations. All the other nanostructured Nb_2O_5 samples show similar distributions. This phenomenon is consistent with hydrogen storage performance of MgH_2 composited with different Nb_2O_5. It is therefore believed that for the catalytic activity of Nb_2O_5, dispersion is the most important factor, which is primarily determined by particle sizes instead of phase structures and morphologies. This is further verified by the fact that the very identical desorption curve to the NP-Nb_2O_5-containing sample was obtained when extending the ball milling duration of the c-Nb_2O_5-containing sample to 24 h because of the more homogeneous and dispersive distribution of catalytic species (Figure S11).

Active catalytic species in Nb_2O_5 modified MgH_2 systems. As observed in Figure 5b, there is an additional low-temperature shift in the dehydrogenation curve of the samples modified with NP-Nb_2O_5, u-Nb_2O_5, f-Nb_2O_5, s-Nb_2O_5 and r-Nb_2O_5 after the first hydrogen cycling. To understand the underlying reasons, we further examined the changes in structure, morphology and composition for the post-cycled samples. Taking MgH_2 modified with NP-Nb_2O_5, f-Nb_2O_5 and r-Nb_2O_5 as representative examples, the distribution of Nb remained nearly the same after 1 desorption/absorption cycle (Figure S12). This therefore rules out the effect of elemental distribution for the further decrease in the desorption temperatures.

XRD examinations identified the diffraction peaks of Nb_2O_5 in the post-milled MgH_2 samples with f-Nb_2O_5, s-Nb_2O_5 and r-Nb_2O_5, especially in the sample with c-Nb_2O_5, as shown in Figure S13, possibly due to their good crystallization and relatively large particle sizes. After 1st desorption and absorption, Nb_2O_5 was still detected in the XRD patterns of the c-Nb_2O_5-modified sample, but its characteristic diffraction peaks became invisible for all the as-synthesized Nb_2O_5 modified samples (Figure 7). This indicates possible reactions between Nb_2O_5 and MgH_2 upon heating. Here, it is noteworthy that the strongest XRD peak of MgO intensified and a new bump at low angle indicates the formation of new compounds. This conjecture was confirmed by reacting high-purity MgH_2 with various Nb_2O_5. As shown in Figure 8a, MgO was not detected in the high-purity MgH_2 before and after ball milling. The strongest characteristic reflection of MgO at 2θ = 42.8° was observed after ball milling MgH_2 with NP-Nb_2O_5 and f-Nb_2O_5 (Figure 8b, c). In stark contrast, Nb_2O_5 was still visible and MgO was not detected when ball milling c-Nb_2O_5 with high-purity MgH_2 (Figure 8d). This indicates that the reaction of NP-Nb_2O_5 and f-Nb_2O_5 with MgH_2 are much easier than c-Nb_2O_5, likely due to their smaller particle size which enhances reactivity. Here, the presence of MgO is unfavorable, which induced the further reduction of hydrogen capacity of the Nb_2O_5-containing samples at the second dehydrogenation (Figure 5b) because of the loss of active Mg element.

The chemical states of Nb at different stages were further examined by XPS. The results are shown in Figure 9. After ball milling with MgH_2, the typical 3p3/2-3p5/2 doublet of Nb in Nb_2O_5 at 209.6 eV and 206.8 eV still dominated the high-resolution XPS spectra for c-Nb_2O_5, NP-Nb_2O_5 and f-Nb_2O_5. At the same time, a new XPS peak appeared at 203.2 eV, which corresponds to NbO.[62] The relative intensity of the NbO peak of the NP-Nb_2O_5 and f-Nb_2O_5-modified sample is distinctly higher than that of the c-Nb_2O_5-containing sample, indicating more reduction of Nb_2O_5,

which agrees well with the XRD results because they identified the formation of MgO. In particular, Nb_2O_5 was further reduced to metallic Nb after 1st dehydrogenation as evidenced by metallic Nb XPS peak at 202.7 eV.[63] The characteristic XPS peaks of Nb_2O_5 nearly disappeared for f-Nb_2O_5 and NP-Nb_2O_5, while they still dominated the XPS spectrum of c-Nb_2O_5. This indicates that nearly all Nb_2O_5 was reduced to Nb(0) after the first (de)hydrogenation cycle for f-Nb_2O_5 and NP-Nb_2O_5 but it was only partially reduced for c-Nb_2O_5. Based upon XRD and XPS results, the reduction levels of Nb_2O_5 are in the order of NP-Nb_2O_5 > f-Nb_2O_5 > c-Nb_2O_5, consistent with observed reduction in desorption temperature. These results indicate that small particle size not only facilitates the uniform distribution of catalytic species, but also promotes the in-situ formation of catalytic species. Thus, we believe that it is particle size not morphology that determines the catalytic activity of Nb_2O_5. This finding will guide the future design and development of high-performance catalysts for hydrogen storage in MgH_2.

Further measurements on hydrogen cycling indicated the stable catalytic effect of NP-Nb_2O_5 because the available hydrogen capacity of MgH_2-7 wt% Nb_2O_5 sample remained at 6.14 wt% after 10 cycles, corresponding to 98.4% of capacity retention (Figure S14a). Moreover, the non-isothermal desorption behaviors remained nearly unchanged after activation (Figure S14b). The stable cycle performance correlates strongly with the structure and composition stability of the composite samples. As shown in Figure S14c and d, no apparent change was observed in the morphology of NP-Nb_2O_5 containing MgH_2 sample. Furthermore, the diffraction peaks of MgH_2 still dominated the XRD profile while several very weak diffraction peaks corresponding to unhydrogenated Mg were also detected, which is responsible for the slight decline in the cycling capacity (Figure S14e). The grain size of MgH_2 was calculated to be 32.2 nm after 10 cycles, which is slightly larger than that of the 1st-dehydrogenated sample (25.2 nm), possibly due to the repeated

heat treatments upon cycling. In addition, the peak intensity of MgO remained almost unchanged, suggesting that the side reaction between Nb_2O_5 and MgH_2 has finished after 1 cycle. This was further confirmed by XPS measurement because of the nearly identical relative intensities of the Nb^0/Nb^{+5} 3d XPS peaks after the 1st and 10th cycle (Figure S14f).

CONCLUSIONS

In this work, six types of Nb_2O_5 with different phase structures, morphologies and sizes including commercial microparticles (c-Nb_2O_5), nanoflowers (f-Nb_2O_5), nanorods (r-Nb_2O_5), hollow spheres (s-Nb_2O_5), urchin-like nanostructures (u-Nb_2O_5) and ultrasmall nanoparticles (NP-Nb_2O_5) were evaluated and compared for their catalytic activities for hydrogen storage in MgH_2. Their catalytic effect was determined to be in the order of NP-Nb_2O_5 > u-Nb_2O_5 > f-Nb_2O_5 ≈ r-Nb_2O_5 ≈ s-Nb_2O_5 > c-Nb_2O_5. In spite of different phase structures and morphologies, f-Nb_2O_5, r-Nb_2O_5 and s-Nb_2O_5 offered nearly identical catalytic efficacy. It is therefore believed that structure and morphology are not the decisive factors for the catalytic activity of Nb_2O_5. In contrast, the particle sizes were measured to be in the order of NP-Nb_2O_5 < u-Nb_2O_5 < f-Nb_2O_5 ≈ r-Nb_2O_5 ≈ s-Nb_2O_5 < c-Nb_2O_5, exhibiting a very good inverse correlation with their catalytic activity. In other words, the catalytic effectiveness of Nb_2O_5 strongly depends on its nanoparticle sizes. The largely reduced particle size contributes to not only the in-situ formation of active catalytic species but also their homogeneous distribution, consequently enabling much higher catalytic activity. Our research reveals the decisive factor of the catalytic activity of Nb_2O_5 for hydrogen storage in Mg/MgH_2, which will help with the design and fabrication of novel catalysts not only for hydrogen storage materials, but also for many other applications such as electrochemical conversion and photosynthesis.

ASSOCIATED CONTENT

Supporting Information.

The Supporting Information is available free of charge at https://pubs.acs.org/doi/

EDS and XPS results of post-milled MgH_2 with and without Nb_2O_5, characterization of p-f-Nb_2O_5, N_2 sorption-desorption isotherms of various Nb_2O_5, dehydrogenation performances of MgH_2 with NP-Nb_2O_5, particle distribution and SEM images of post-milled MgH_2 with and without NP-Nb_2O_5, TPD-MS curves and Kissinger's plots of MgH_2 with various Nb_2O_5 at the first and second cycles, SEM image and EDS mapping of r-Nb_2O_5-containing MgH_2, BSE images of MgH_2 with Nb_2O_5, TEM images and EDS mappings of post-milled MgH_2 with various Nb_2O_5, dehydrogenation performance and EDS mappings of the post-24 h milled c-Nb_2O_5-containing MgH_2, TEM images and EDS mappings of MgH2 with various Nb_2O_5 after the 1st hydrogenation, XRD patterns of the post-milled Nb_2O_5-containing MgH_2, cycling behaviors and changes in particle sizes, microstructures and chemical states of MgH_2 with NP-Nb_2O_5 after 10 cycles, and summary of crystal structure and morphology of various Nb_2O_5. (PDF)

AUTHOR INFORMATION

Corresponding Author

Yongfeng Liu - State Key Laboratory of Silicon Materials and School of Materials Science and Engineering, Zhejiang University, Hangzhou 310027, China; Institute of Science and Technology for New Energy, Xi'an Technological University, Xi'an, 710021, China; Email: mselyf@zju.edu.cn

Hongge Pan - State Key Laboratory of Silicon Materials and School of Materials Science and Engineering, Zhejiang University, Hangzhou 310027, China; Institute of Science and Technology for New Energy, Xi'an Technological University, Xi'an, 710021, China; Email: hgpan@zju.edu.cn

Author Contributions

The manuscript was written through contributions of all authors. All authors have given approval to the final version of the manuscript. ‡These authors contributed equally.

Notes

The authors declare no competing financial interest.

ACKNOWLEDGMENT

We gratefully acknowledge the financial support received from the National Key R&D Program of China (2022YFB3803700), the National Outstanding Youth Foundation of China (52125104), the Natural Science Foundation of Zhejiang Province (LD21E010002), the National Natural Science Foundation of China (52001277, U22A20120), the Fundamental Research Funds for the Central Universities (2021FZZX001-09, 226-2022-00246), and the National Youth Top-Notch Talent Support Program.

REFERENCES

[1] Odenweller, A.; Ueckerdt, F.; Nemet, G. F.; Jensterle, M.; Luderer, G. Probabilistic Feasibility Space of Scaling up Green Hydrogen Supply. *Nature Energy* **2022**, *7*, 854−865.

[2] Net Zero by 2050 (IEA, 2021); https://www.iea.org/reports/net-zero-by-2050.

[3] Van Renssen, S. The Hydrogen Solution? *Nature Climate Change* **2020**, *10*, 799−801.

[4] Schlapbach, L.; Züttel, A. Hydrogen-Storage Materials for Mobile Applications. *Nature* **2001**, *414*, 353−358.

[5] He, T.; Pachfule, P.; Wu, H.; Xu, Q.; Chen, P. Hydrogen Carriers. *Nature Rev. Mater*. **2016**, *1*, 16059.

[6] Allendorf, M.; Stavila, V.; Snider, J. L.; Witman, M.; Bowden,M. E.; Brooks, K.; Tran, B. L.; Autrey, T. Challenges to Developing Materials for the Transport and Storage of Hydrogen. *Nat. Chem*. **2022**, *14*, 1214−1223.

[7] Eberle, U.; Felderhoff, M.; Schüth, F. Chemical and Physical Solutions for Hydrogen Storage. *Angew. Chem. Int. Ed*. **2009**, *48*, 6608−6630.

[8] Bérubé, V.; Radtke, G.; Dresselhaus, M.; Chen, G. Size Effects on the Hydrogen Storage Properties of Nanostructured Metal Hydrides: A review. *Int. J. Energy Res*. **2007**, *31*, 637−663.

[9] Sakintuna, B.; Lamari-Darkrim, F.; Hirscher, M. Metal Hydride Materials for Solid Hydrogen Storage: A review. *Int. J. Hydrogen Energy* **2007**, *32*, 1121−1140.

[10] Mohtadi, R.; Orimo, S. The Renaissance of Hydrides as Energy Materials. *Nat. Rev. Mater*. **2017**, *2*, 16091.

[11] Tan, K. C.; Yu, Y.; Chen, R.; He, T.; Jing, Z.; Pei, Q.; Wang, J.; Chua, Y. S.; Wu, A.; Zhou, W.; Wu, H.; Chen, P. Metallo-N-Heterocycles - A New Family of Hydrogen Storage Material. *Energy Storage Mater*. **2020**, *26*, 198−202.

[12] Zheng, J.; Zhou, H.; Wang, C. G.; Ye, E.; Xu, J. W.; Loh, X. J.; Li, Z. B. Current Research Progress and Perspectives on Liquid Hydrogen Rich Molecules in Sustainable Hydrogen Storage. *Energy Storage Mater*. **2021**, *35*, 695−722.

[13] Gupta, A.; Baron, G. V.; Perreault, P.; Lenaerts, S.; Ciocarlan, R.-G.; Cool, P.; Mileo, P. G. M.; Rogge, S.; Van Speybroeck, V.; Watson, G.; Van Der Voort, P.; Houlleberghs, M.; Breynaert, E.; Martens, J.; Denayer, J. F. M. Hydrogen Clathrates: Next Generation Hydrogen Storage Materials. *Energy Storage Mater*. **2021**, *41*, 69−107.

[14] Chandra, D.; Reilly, J. J.; Chellappa, R. Metal Hydrides for Vehicular Applications: The State of the Art. *JOM* **2006**, *58*, 26−32.

[15] Liu, Y. F.; Pan, H. G.; Gao, M. X.; Wang, Q. D. Advanced Hydrogen Storage Alloys for Ni/MH Rechargeable Batteries. *J. Mater. Chem*. **2011**, *21*, 4743−4755.

[16] Ngene, P.; Longo, A.; Mooij, L.; Dam, B. Metal-hydrogen Systems with an Exceptionally Large and Tunable Thermodynamic Destabilization. *Nature Commun*. **2017**, *8*, 1846.

[17] Tarasov, B. P.; Fursikov, P. V.; Volodin, A. A.; Bocharnikov, M. S.; Shimkus,Y. Y.; Kashin, A. M.; Yartys, V. A.; Chidziva, S.; Pasupathi, S.; Lototskyy, M. V. Metal Hydride Hydrogen Storage and Compression Systems for Energy Storage Technologies. *Int. J. Hydrogen Energy* **2021**, *46*, 13647−13657.

[18] Aguey-Zinsou, K. F.; Ares-Fernández, J. R. Hydrogen in Magnesium: New Perspectives Toward Functional Stores. *Energy Environ. Sci*. **2010**, *3*, 526−543.

[19] Jain, I. P.; Lal, C.; Jain, A. Hydrogen storage in Mg: A Most Promising Material. *Int. J. Hydrogen Energy* **2010**, *35*, 5133−5144.

[20] Yartys, V. A.; Lototskyy, M. V.; Akiba, E.; Albert, R.; Antonov, V. E.; Ares, J. R.; Baricco, M.; Bourgeois, N.; Buckley, C. E.; von Colbe, J. M. B.; Crivello, J. C.; Cuevas, F.; Denys, R. V.; Dornheim, M.; Felderhoff, M.; Grant, D. M.; Hauback, B. C.; Humphries, T. D.; Jacob, I.; Jensen, T. R.; de Jongh, P. E.; Joubert, J. M.; Kuzovnikov, M. A.; Latroche, M.; Paskevicius, M.; Pasquini, L.; Popilevsky, L.; Skripnyuk, V. M.; Rabkin, E.; Sofianos, M. V.; Stuart, A.;

Walker, G.; Wang, H.; Webb, C. J.; Zhu, M. Magnesium Based Materials for Hydrogen Based Energy Storage: Past, Present and Future. *Int. J. Hydrogen Energy* **2019**, *44*, 7809−7859.

[21] Zhang, X. L.; Liu, Y. F.; Zhang, X.; Hu, J. J.; Gao, M. X.; Pan, H. G. Empowering Hydrogen Storage Performance of MgH_2 by Nanoengineering and Nanocatalysis. *Mater. Today Nano* **2020**, *9*, 100064.

[22] Sun, Y.; Shen, C.; Lai, Q.; Liu, W.; Wang, D. W.; Aguey-Zinsou, K. F. Tailoring Magnesium-Based Materials for Hydrogen Storage Through Synthesis: Current State of the Art. *Energy Storage Mater.* **2018**, *10*, 168−198.

[23] Salman, M. S.; Pratthana, C.; Lai, Q.; Wang, T.; Rambhujun, N.; Srivastava, K.; Aguey-Zinsou, K.-F. Catalysis in Solid Hydrogen Storage: Recent Advances, Challenges, and Perspectives. *Energy Technol*. **2022**, *10*, 2200433.

[24] Yang, Y.X.; Zhang, X.; Zhang, L.C.; Zhang, W.X.; Liu, H.F.; Huang, Z. G.; Yang, L. M.; Gu, C. D.; Sun, W. P.; Gao, M. X.; Liu, Y. F.; Pan, H. G. Recent Advances in Catalyst-Modified Mg-Based Hydrogen Storage Materials. *J. Mater. Sci. Technol.* **2023**, *163*, 182−211.

[25] Webb, C. J. A review of Catalyst-Enhanced Magnesium Hydride as a Hydrogen Storage Material. *J. Phys. Chem. Solids* **2015**, *84*, 96−106.

[26] Liang, G.; Huot, J.; Boily, S.; Neste, A.; Schulz, R. Catalytic Effect of Transition Metals on Hydrogen Sorption in Nanocrystalline Ball Milled MgH_2-Tm (Tm = Ti, V, Mn, Fe and Ni) Systems. *J. Alloy. Compd*. **1999**, *292*, 247−252.

[27] Chen, J.; Xia, G. L.; Guo, Z. P.; Huang, Z. G.; Liu, H. K.; Yu, X. B. Porous Ni Nanofibers with Enhanced Catalytic Effect on the Hydrogen Storage Performance of MgH_2. *J. Mater. Chem. A* **2015**, *3*, 15843−15848.

[28] Lu, Z. Y.; Yu, H. J.; Lu, X.; Song, M. C.; Wu, F. Y.; Zheng, J. G.; Yuan, Z. F.; Zhang, L. T. Two-Dimensional Vanadium Nanosheets as a Remarkably Effective Catalyst for Hydrogen Storage in MgH_2. *Rare Met*. **2021**, *40*, 3195−3204.

[29] Zhang, L. T.; Cai, Z. L.; Yao, Z. D.; Ji, L.; Sun, Z.; Yan, N. H.; Zhang, B. Y.; Xiao, B. B.; Du, J.; Zhu, X. Q.; Chen, L. X. A Striking Catalytic Effect of Facile Synthesized $ZrMn_2$ Nanoparticles on the De/Rehydrogenation Properties of MgH_2. *J. Mater. Chem. A* **2019**, *7*, 5626−5634.

[30] El-Eskandarany, M. S. Metallic Glassy Ti_2Ni Grain-Growth Inhibitor Powder for Enhancing the Hydrogenation/Dehydrogenation Kinetics of MgH_2. *RSC Adv*. **2019**, *9*, 1036−1046.

[31] Verma, S. K.; Bhatnagar, A.; Shukla, V.; Soni, P. K.; Pandey, A. P.; Yadav, T. P.; Srivastava, O. N. Multiple Improvements of Hydrogen Sorption and Their Mechanism for MgH_2 Catalyzed Through TiH_2@Gr. *Int. J. Hydrogen Energy* **2020**, *45*, 19516−19530.

[32] El-Eskandarany, M. S.; Shaban, E.; Al-Matrouk, H.; Behbehani, M.; Alkandary, A.; Aldakheel, F.; Ali, N.; Ahmed, S. A. Structure, Morphology and Hydrogen Storage Kinetics of Nanocomposite MgH_2/10 wt% $ZrNi_5$ Powders. *Mater. Today Energy* **2017**, *3*, 60−71.

[33] Shokano, G.; Dehouche, Z.; Galey, B.; Postole, G. Development of a Novel Method for the Fabrication of Nanostructured $Zr_{(x)}Ni_{(y)}$ Catalyst to Enhance the Desorption Properties of MgH_2. *Catalysts* **2020**, *10*, 849.

[34] Chen, M.; Yi, Y. Q.; Xiao, X. Z.; Lu, Y. H.; Zhang, M.; Zheng, J. G.; Chen, L. X. Highly Efficient ZrH_2 Nanocatalyst for the Superior Hydrogenation Kinetics of Magnesium Hydride Under Moderate Conditions: Investigation and Mechanistic Insights. *Appl. Surf. Sci*. **2021**, *541*, 148375.

[35] Zhang, X. L.; Zhang, X.; Zhang, L. C.; Huang, Z. G.; Fang, F.; Yang, Y. X.; Gao, M. X.; Pan, H. G.; Liu, Y. F. Remarkable Low-Temperature Hydrogen Cycling Kinetics of Mg Enabled by VH_x Nanoparticles. *J. Mater. Sci. Tech*. **2023**, *144*, 168−177.

[36] Rizo-Acosta, P.; Cuevas, F.; Latroche, M. Hydrides of Early Transition Metals as Catalysts and Grain Growth Inhibitors for Enhanced Reversible Hydrogen Storage in Nanostructured Magnesium. *J. Mater. Chem. A* **2019**, *7*, 23064−23075.

[37] Pighin, S. A.; Coco, B.; Troiani, H.; Castro, F. J.; Urretavizcaya, G. Effect of Additive Distribution in H_2 Absorption and Desorption Kinetics in MgH_2 Milled with $NbH_{0.9}$ or NbF_5. *Int. J. Hydrogen Energy* **2018**, *43*, 7430−7439.

[38] Kumar, S.; Jain, A.; Yamaguchi, S.; Miyaoka, H.; Ichikawa, T.; Mukherjee, A.; Dey, G. K.; Kojima, Y. Surface Modification of MgH_2 by $ZrCl_4$ to Tailor the Reversible Hydrogen Storage performance. *Int. J. Hydrogen Energy* **2017**, *42*, 6152−6159.

[39] Ma, L. P.; Kang, X. D.; Dai, H. B.; Liang, Y.; Fang, Z. Z.; Wang, P. J.; Wang, P.; Cheng, H. M. Superior Catalytic Effect of TiF_3 over $TiCl_3$ in Improving the Hydrogen Sorption Kinetics of MgH_2: Catalytic Role of Fluorine Anion. *Acta Mater*. **2009**, *57*, 2250−2258.

[40] Chen, M.; Xiao, X. Z.; Zhang, M.; Mao, J. F.; Zheng, J. G.; Liu, M. J.; Wang, X. C.; Chen, L. X. Insights into 2D Graphene-Like TiO_2 (B) Nanosheets as Highly Efficient Catalyst for Improved Low-Temperature Hydrogen Storage Properties of MgH_2. *Mater. Today Energy* **2020**, *16*, 100411.

[41] Zhang, X. L.; Zhang, X.; Zhang, L. C.; Huang, Z. G.; Fang, F.; Hu, J. J.; Yang, Y. X.; Gao, M. X.; Pan, H. G.; Liu, Y.F. Ultrafast Hydrogenation of Magnesium Enabled by Tetragonal ZrO_2 Hierarchical Nanoparticles. *Mater. Today Nano* **2022**, *18*, 100200.

[42] Wang, K.; Zhang, X.; Ren, Z. H.; Zhang, X. L.; Hu, J. J.; Gao, M. X.; Pan, H. G.; Liu, Y. F. Nitrogen-Stimulated Superior Catalytic Activity of Niobium Oxide for Fast Full Hydrogenation of Magnesium at Ambient Temperature. *Energy Storage Mater*. **2019**, *23*, 79−87.

[43] Yang, B.; Zou, J. X.; Huang, T. P.; Mao, J. F.; Zeng, X. Q.; Ding, W. J.; Enhanced Hydrogenation and Hydrolysis Properties of Core-shell Structured Mg-MO_x (M= Al, Ti and Fe) Nanocomposites Prepared by Arc Plasma Method. *Chem. Eng. J*. **2019**, *371*, 233−243.

[44] Ren, L.; Zhu, W.; Li, Y. H.; Lin, X.; Xu, H.; Sun, F. Z.; Lu, C.; Zou, J. X.; Oxygen Vacancy-Rich 2D TiO_2 Nanosheets: A Bridge Toward High Stability and Rapid Hydrogen Storage Kinetics of Nano-Confined MgH_2. *Nano-Micro Lett*. **2022**, *14*, 5193.

[45] Wang, Z. Y.; Ren, Z. H.; Jian, N.; Gao, M. X.; Hu, J. J.; Du, F.; Pan, H. G.; Liu, Y. F. Vanadium Oxide Nanoparticles Supported on Cubic Carbon Nanoboxes as Highly Active Catalyst Precursors for Hydrogen Storage in MgH_2. *J. Mater. Chem. A* **2018**, *6*, 16177−16185.

[46] Liu, Y. N.; Gao, H. G.; Zhu, Y. F.; Li, S. Y.; Zhang, J. G.; Li, L. Q. Excellent Catalytic Activity of a Two-Dimensional $Nb_4C_3T_x$ (MXene) on Hydrogen Storage of MgH_2. *Appl. Surf. Sci*. **2019**, *493*, 431−440.

[47] Liu, Y. F.; Du, H. F.; Zhang, X.; Yang, Y. X.; Gao, M. X.; Pan, H. G. Superior Catalytic Activity Derived from Two-Dimensional Ti_3C_2 Precursor Towards the Hydrogen Storage Reaction of Magnesium Hydride. *Chem. Commun*. **2016**, *52*, 705−708

[48] Wang, P.; Tian, Z. H.; Wang, Z. X.; Xia, C. Q.; Yang, T.; Ou, X. L. Improved Hydrogen Storage Properties of MgH_2 Using Transition Metal Sulfides as Catalyst. *Int. J. Hydrogen Energy* **2021**, *46*, 27107−27118.

[49] Xie, X. B.; Ma, X. J.; Liu, P.; Shang, J. X.; Li, X. G.; Liu, T. Formation of Multiple-Phase Catalysts for the Hydrogen Storage of Mg Nanoparticles by Adding Flowerlike NiS. *ACS Appl. Mater. Interfaces* **2017**, *9*, 5937−5946.

[50] Wang, Z. X.; Tian, Z. H.; Yao, P. F.; Zhao, H. M.; Xia, C. Q.; Yang, T. Improved Hydrogen Storage Kinetic Properties of Magnesium-Based Materials by Adding Ni_2P. *Renew. Energy* **2022**, *189*, 559−569.

[51] Zhang, M.; Xiao, X. Z.; Hang, Z. M.; Chen, M.; Wang, X. C.; Zhang, N.; Chen, L. X. Superior Catalysis of NbN Nanoparticles with Intrinsic Multiple Valence on Reversible Hydrogen Storage Properties of Magnesium Hydride. *Int. J. Hydrogen Energy* **2021**, *46*, 814−822.

[52] Amirkhiz, B. S.; Danaie, M.; Barnes, M.; Simard, B.; Mitlin, D. Hydrogen Sorption Cycling Kinetic Stability and Microstructure of Single-Walled Carbon Nanotube (SWCNT) Magnesium Hydride (MgH_2) Nanocomposites. *J. Phys. Chem. C* **2010**, *114*, 3265−3275.

[53] Liu, G.; Wang, Y. J.; Xu, C. C.; Qiu, F. Y.; An, C. H.; Li, L.; Jiao, L. F.; Yuan, H. T. Excellent Catalytic Effects of Highly Crumpled Graphene Nanosheets on Hydrogenation/Dehydrogenation of Magnesium Hydride. *Nanoscale* **2013**, *5*, 1074−1081.

[54] Liu, G.; Wang, Y. J.; Jiao, L. F.; Yuan, H. T. Understanding the Role of Few-Layer Graphene Nanosheets in Enhancing the Hydrogen Sorption Kinetics of Magnesium Hydride. *ACS Appl. Mater. Interfaces* **2014**, *6*, 11038−11046.

[55] Zhang, L. T.; Chen, L. X.; Fan, X. L.; Xiao, X. Z.; Zheng, J. G.; Huang, X. Enhanced Hydrogen Storage Properties of MgH_2 with Numerous Hydrogen Diffusion Channels Provided by $Na_2Ti_3O_7$ Nanotubes. *J. Mater. Chem. A* **2017**, *5*, 6178−6185.

[56] Zhang, H. H.; Kong, Q. Q.; Hu, S.; Zhang, D. F.; Chen, H. P.; Xu, C. C.; Li, B. J.; Fan, Y. P.; Liu, B. Z. Engineering the Oxygen Vacancies in $Na_2Ti_3O_7$ for Boosting Its Catalytic Performance in MgH_2 Hydrogen Storage. *ACS Sustain. Chem. Eng*. **2022**, *10*, 363−371.

[57] Zhang, M.; Xiao, X. Z.; Wang, X. W.; Chen, M.; Lu, Y. H.; Liu, M. J.; Chen, L. X. Excellent Catalysis of TiO_2 Nanosheets with High-Surface-Energy {001} Facets on the Hydrogen Storage Properties of MgH_2. *Nanoscale* **2019**, *11*, 7465−7473.

[58] Zhang, L. C.; Wang, K.; Liu, Y. F.; Zhang, X.; Hu, J. J.; Gao, M. X.; Pan, H. G. Highly Active Multivalent Multielement Catalysts Derived from Hierarchical Porous $TiNb_2O_7$ Nanospheres for the Reversible Hydrogen Storage of MgH_2. *Nano Res*. **2021**, *14*, 148−156.

[59] Xian, K. C.; Wu, M. H.; Gao, M. X.; Wang, S.; Li, Z. L.; Gao, P. Y.; Yao, Z. H.; Liu, Y. F.; Sun, W. P.; Pan, H. G. A Unique Nanoflake-Shape Bimetallic Ti-Nb Oxide of Superior Catalytic Effect for Hydrogen Storage of MgH_2. *Small* **2022**, *18*, 2107013.

[60] Zhang, X. L.; Wang, K.; Zhang, X.; Hu, J. J.; Gao, M. X.; Pan, H. G.; Liu, Y. F. Synthesis Process and Catalytic Activity of Nb_2O_5 Hollow Spheres for Reversible Hydrogen Storage of MgH_2. *Int J Energy Res*. **2020**, *45*, 3129−3141.

[61] Fan, W. Q.; Zhang, Q. H.; Deng, W. P.; Wang, Y. Niobic Acid Nanosheets Synthesized by a Simple Hydrothermal Method as Efficient Brønsted Acid Catalysts. *Chem. Mater*. **2013**, *25*, 3277−3187.

[62] Lewandków, R.; Mazur, P.; Grodzicki, M. Niobium Oxides Films on GaN: Photoelectron Spectroscopy study. *Thin Solid Films* **2022**, *763*, 139573

[63] Hryniewicz, T.; Rokosz, K.; Sandim, H. R. Z. SEM/EDX and XPS Studies of Niobium after Electropolishing. *Appl. Surf. Sci*. **2012**, *263*, 357−361.

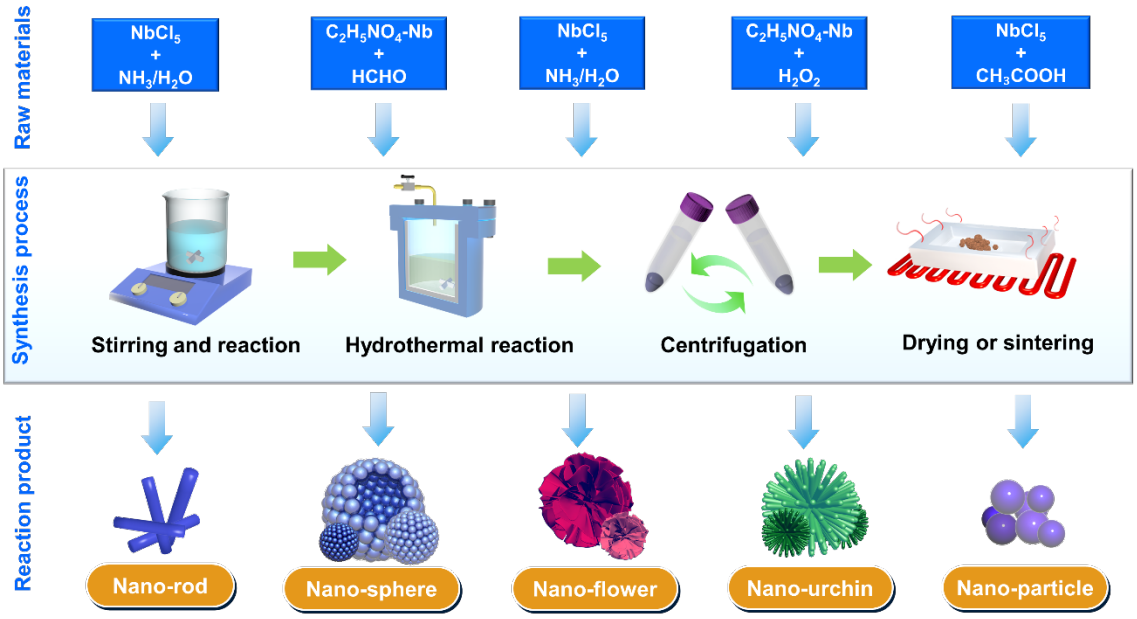

Figure 1. Schematic synthesis process of Nb_2O_5 nanocatalysts with different morphologies.

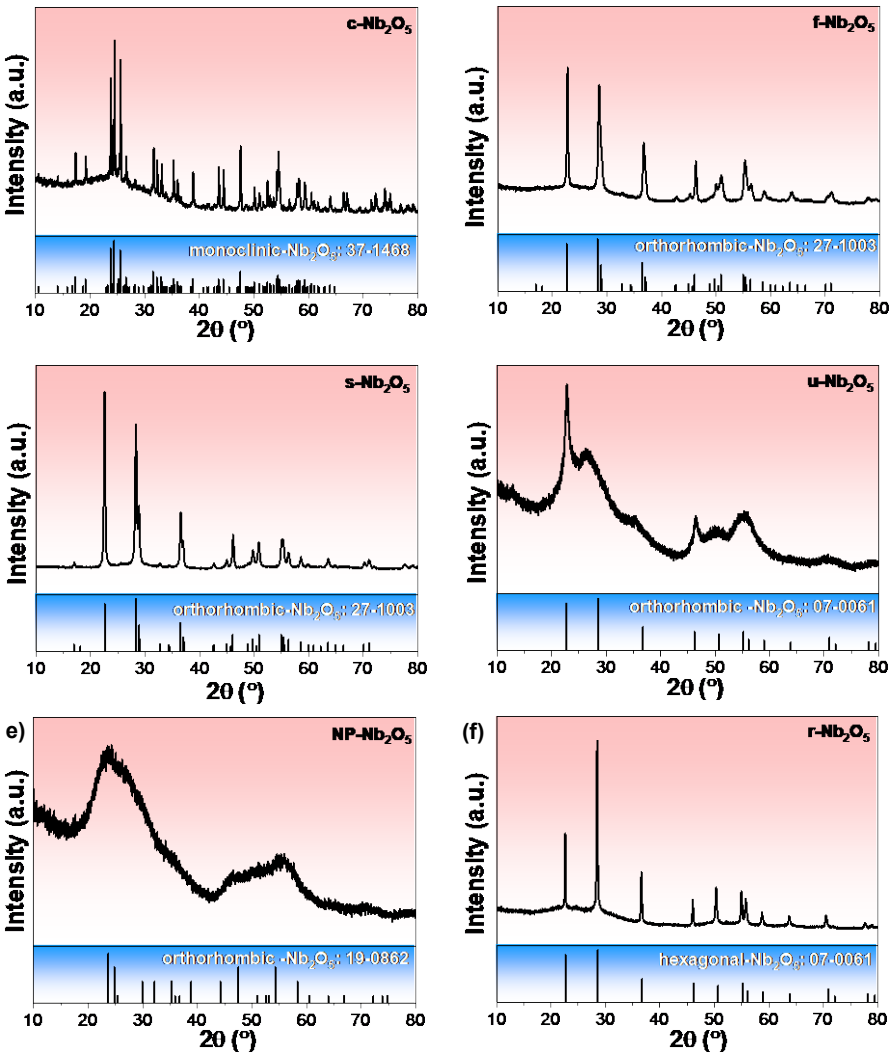

Figure 2. XRD patterns of commercial Nb_2O_5 (a); and the as-synthesized Nb_2O_5 with different morphologies: nanoflowers (b); hollow spheres (c); urchin shape (d); nanoparticles (e); and nanorods (f).

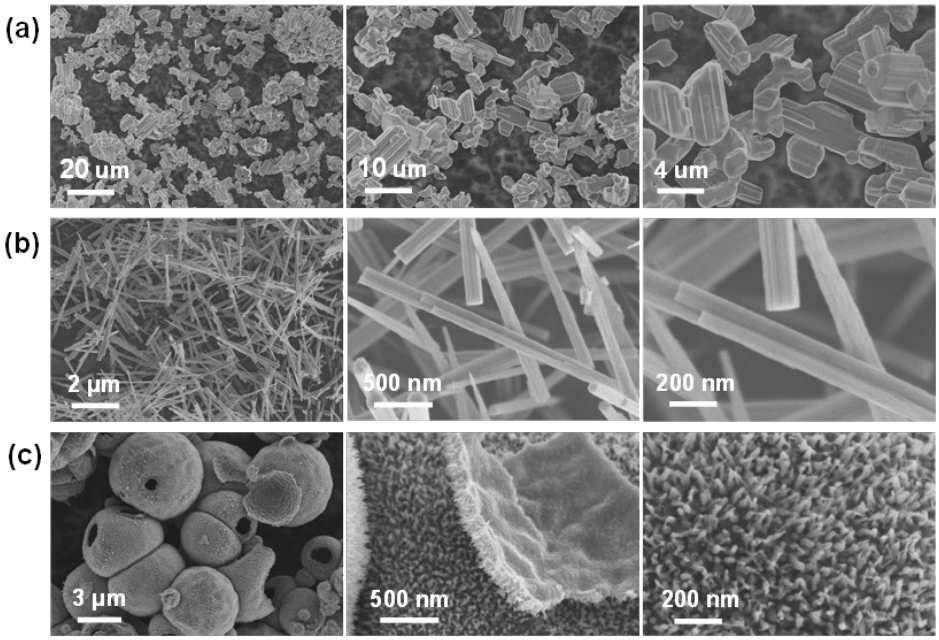

Figure 3. SEM images of c-Nb_2O_5 (a); r-Nb_2O_5 (b); and s-Nb_2O_5 (c).

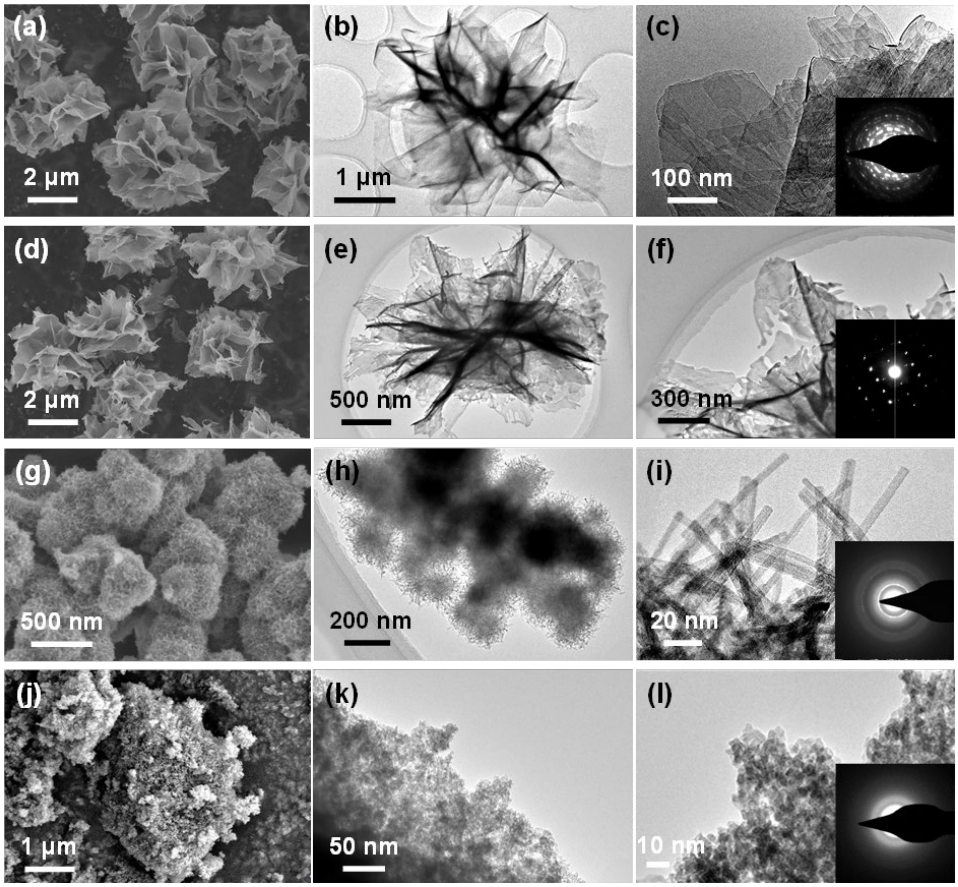

Figure 4. SEM (a, d, g, j); and TEM (b-c, e-f, h-i, k-l) images of p-f-Nb_2O_5 (a-c); f-Nb_2O_5 (d-f); u-Nb_2O_5 (g-i); and NP-Nb_2O_5 (j-l). The insets in (c), (f), (i) and (l) are corresponding SAED patterns.

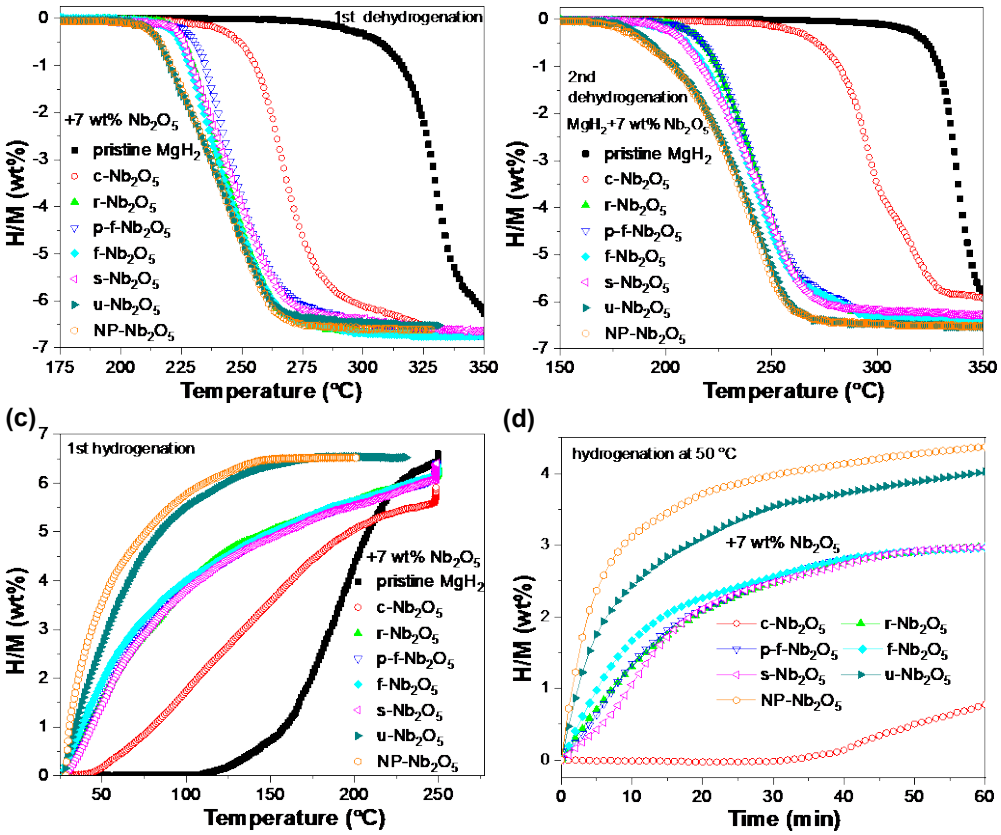

Figure 5. Comparison of the 1st dehydrogenation curves (a); 2nd dehydrogenation curves (b); 1st hydrogenation curves (c); and the isothermal hydrogenation curves (d) at 50 °C under 50 bar H_2, for MgH_2 ball milled with different Nb_2O_5 catalysts.

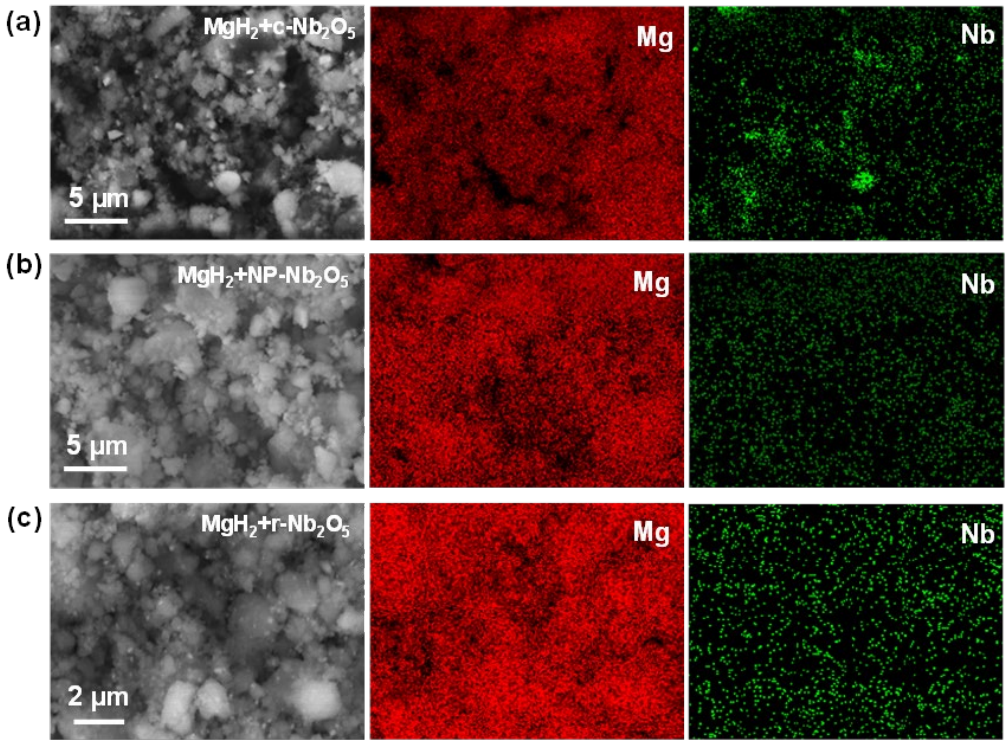

Figure 6. SEM and corresponding EDS mappings of Mg and Nb elements in c-Nb_2O_5 (a); NP-Nb_2O_5 (b); r-Nb_2O_5 (c) containing MgH_2 samples.

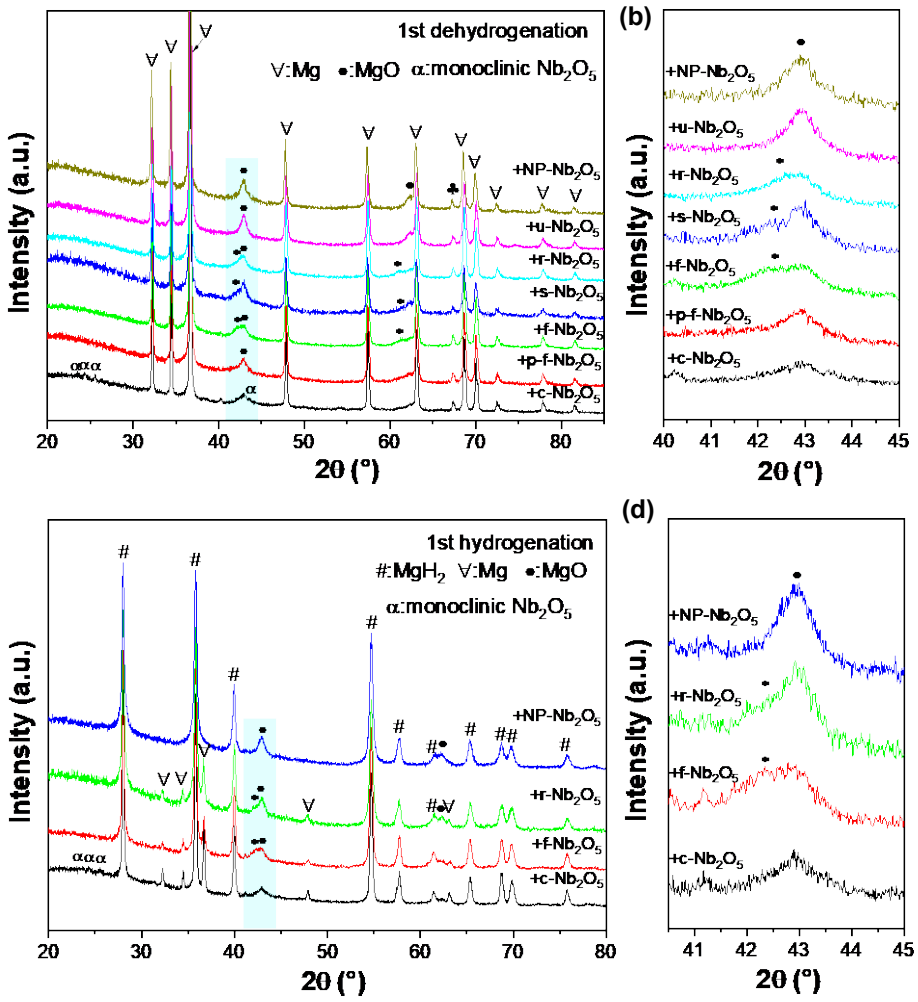

Figure 7. XRD patterns of Nb_2O_5 modified MgH_2 after the 1st dehydrogenation (a-b); and 1st hydrogenation (c-d). (b) and (d) are the enlarged patterns at the range of 40.5-45° in (a) and (c), respectively.

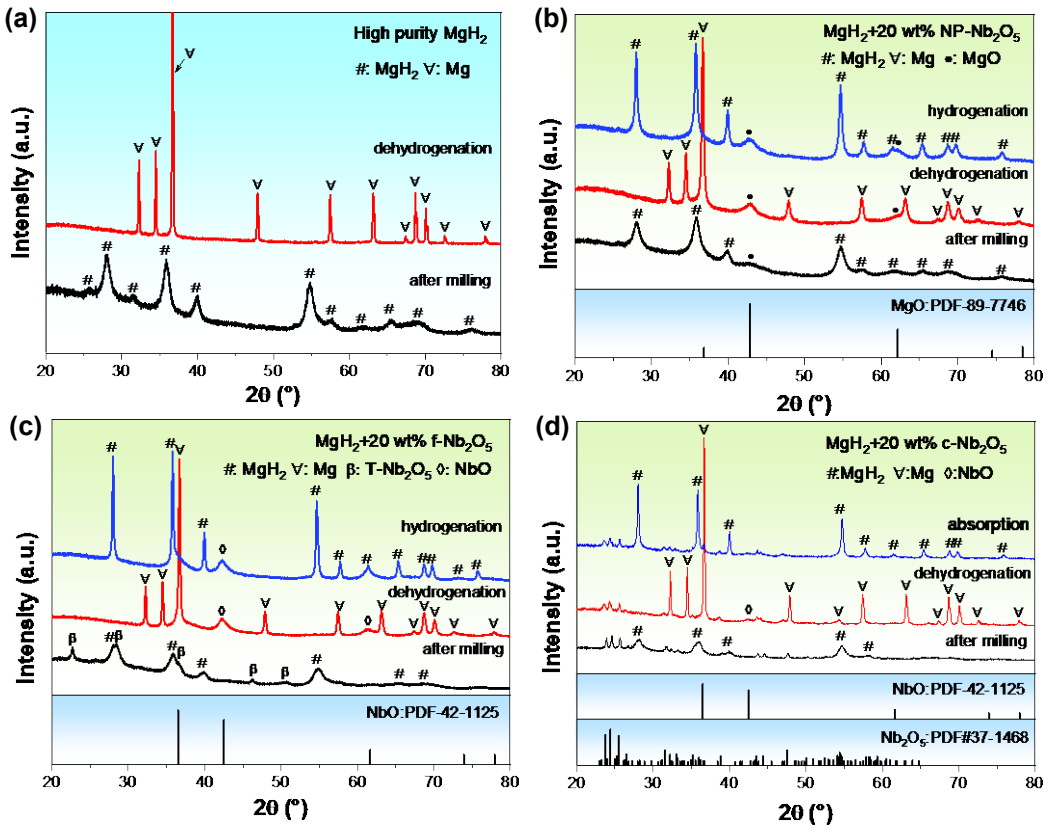

Figure 8. XRD patterns of MgH_2 (a), MgH_2+20 wt% NP-Nb_2O_5 (b), MgH_2+20 wt% f-Nb_2O_5 (c) and MgH_2+20 wt% c-Nb_2O_5 (d) at different stages.

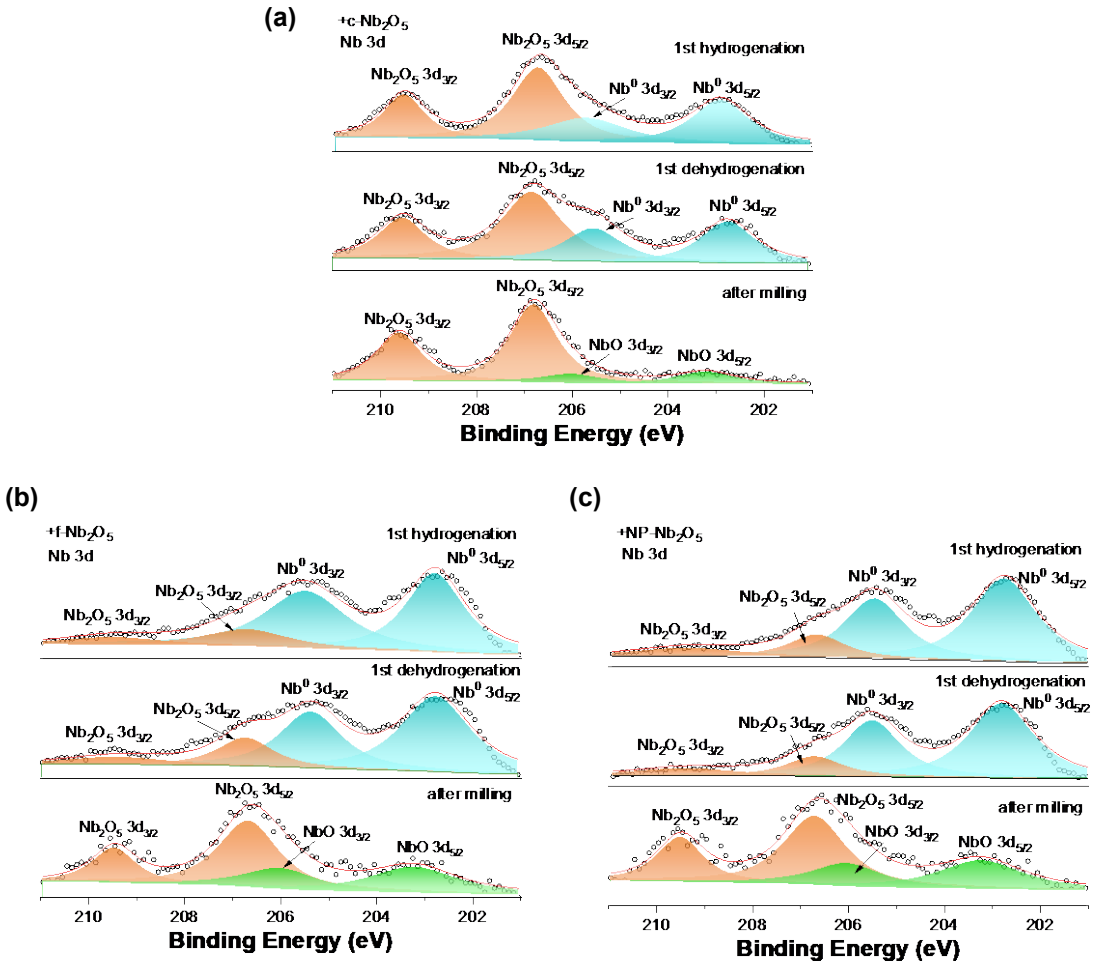

Figure 9. XPS spectra of Nb in MgH_2+7 wt% c-Nb_2O_5 (a); MgH_2+7 wt% f-Nb_2O_5 (b); and MgH_2+7 wt% NP-Nb_2O_5 (c) at different stages. (black circle curves: original data curves, red line curves: fitting line, orange peaks: Nb(+5) spin-orbit peaks in Nb_2O_5, green peaks: Nb(+2) spin-orbit peaks in NbO, cyan peaks: Nb^0 spin-orbit peaks)